Draft version August 27, 2021
Typeset using LATEX twocolumn style in AASTeX631

Simulations of helical inflationary magnetogenesis and gravitational waves

Axel Brandenburg,[1,2,3,4] Yutong He,[1,2] and Ramkishor Sharma[5]

[1]Nordita, KTH Royal Institute of Technology and Stockholm University, Hannes Alfvéns väg 12, SE-10691 Stockholm, Sweden
[2]Department of Astronomy, AlbaNova University Center, Stockholm University, SE-10691 Stockholm, Sweden
[3]McWilliams Center for Cosmology & Department of Physics, Carnegie Mellon University, Pittsburgh, PA 15213, USA
[4]School of Natural Sciences and Medicine, Ilia State University, 3-5 Cholokashvili Avenue, 0194 Tbilisi, Georgia
[5]Inter University Centre for Astronomy and Astrophysics, Post Bag 4, Pune University Campus, Ganeshkhind, Pune 411 007, India

ABSTRACT

Using numerical simulations of helical inflationary magnetogenesis in a low reheating temperature scenario, we show that the magnetic energy spectrum is strongly peaked at a particular wavenumber that depends on the reheating temperature. Gravitational waves (GWs) are produced at frequencies between 3 nHz and 50 mHz for reheating temperatures between 150 MeV and 3×10^5 GeV, respectively. At and below the peak frequency, the stress spectrum is always found to be that of white noise. This implies a linear increase of GW energy per logarithmic wavenumber interval, instead of a cubic one. Both in the helical and nonhelical cases, the GW spectrum is followed by a sharp drop for frequencies above the respective peak frequency. In this magnetogenesis scenario, the presence of a helical term extends the peak of the GW spectrum and therefore also the position of the aforementioned drop toward larger frequencies compared to the case without helicity. This might make a difference in it being detectable with space interferometers. The efficiency of GW production is found to be almost the same as in the nonhelical case, and independent of the reheating temperature, provided the electromagnetic energy at the end of reheating is fixed to be a certain fraction of the radiation energy density. Also, contrary to the case without helicity, the electric energy is now less than the magnetic energy during reheating. The fractional circular polarization is found to be nearly hundred per cent in a certain range below the peak frequency range.

Keywords: gravitational waves—early Universe—turbulence—magnetic fields—MHD

1. INTRODUCTION

There has been significant interest in the production of helical magnetic fields and circularly polarized gravitational waves (GWs) from the early Universe (Garretson et al. 1992; Cornwall 1997; Vachaspati 2001; Kahniashvili et al. 2005, 2021; Anber & Sorbo 2006; Campanelli 2009; Durrer et al. 2011; Durrer & Neronov 2013; Caprini & Sorbo 2014; Subramanian 2016; Adshead et al. 2016, 2018). Owing to magnetic helicity conservation, such fields would have had a better chance to survive until the present time (Christensson et al. 2001; Banerjee & Jedamzik 2004; Kahniashvili et al. 2016; Brandenburg et al. 2017). The associated electromagnetic (EM) stress also drives circularly polarized GWs (Kahniashvili et al. 2005, 2021; Ellis et al. 2020; Roper Pol et al. 2021). If the sign and spectral shape of the circular polarization can in future be detected, it would provide important information about the underlying mechanisms responsible for the generation.

Inflationary magnetogenesis scenarios are particularly attractive, because they have the advantage of producing large-scale magnetic fields. They tend to amplify magnetic fields from quantum fluctuations by the breaking of conformal invariance through a function f such that the Lagrangian density has a term that takes the form $f^2F_{\mu\nu}F^{\mu\nu}$, where $F_{\mu\nu}$ is the Faraday tensor (Turner & Widrow 1988; Ratra 1992). However, those mechanisms can only be viable if they avoid some well-known problems discussed in detail in the literature (Demozzi et al. 2009; Ferreira et al. 2013; Kobayashi & Afshordi 2014; Kobayashi & Sloth

Corresponding author: Axel Brandenburg
brandenb@nordita.org

2019). These problems are avoided by requiring the function f to obey certain constraints that have been discussed in detail by Sharma et al. (2017). For some scenarios, these magnetic fields can lead to the production of GWs which lie in the sensitivity range of space interferometers such as LISA and Taiji, as studied analytically in Sharma et al. (2020). This magnetogenesis model was also extended to the helical case (Sharma et al. 2018, hereafter referred to as SSS). A similar model of helical magnetogenesis was considered by Fujita & Durrer (2019) and Okano & Fujita (2021). Numerical simulations have recently been performed for the nonhelical case (Brandenburg & Sharma 2021, hereafter BS). The goal of the present paper is to apply numerical simulations now to helical magnetogenesis. These models continue to amplify EM fields during the post-inflationary matter-dominated era after inflation, but require relatively low reheating temperatures, $T_{\rm r}$. Values of $T_{\rm r}$ in the range of the electroweak and quantum chromodynamics (QCD) epochs are often discussed, but do not have to coincide with them. Here we consider values of $T_{\rm r}$ in the range from $150\,{\rm MeV}$ to $3\times10^5\,{\rm GeV}$, which correspond to peak frequencies of GWs in the ranges accessible to pulsar timing arrays (Detweiler 1979; Hobbs et al. 2010; Arzoumanian et al. 2020) and space interferometers (Caprini et al. 2016; Amaro-Seoane et al. 2017; Taiji Scientific Collaboration et al. 2021).

As in Sharma et al. (2017) and SSS, we assume that f is a function of the scale factor a with $f(a)\propto a^{\alpha}$ during inflation, and $f(a)\propto a^{-\beta}$ during the post-inflationary matter-dominated era, where $\alpha=2$ was fixed and β is an exponent whose value depends on $T_{\rm r}$. The magnetic field becomes unstable and is rapidly amplified at large length scales, provided the second derivative of f with respect to conformal time is positive. This can be the case both for positive and negative exponents, i.e., both during and after inflation, but no longer in the radiation dominated era, where $f=1$ must be obeyed for standard (conformally invariant) electromagnetism to hold.

In contrast to BS, we now consider an additional term $\gamma f^2 F_{\mu\nu}\tilde{F}^{\mu\nu}$ in the Lagrangian density, where γ is a constant and $\tilde{F}^{\mu\nu}$ is the dual of the Faraday tensor. The product is proportional to $\mathbf{E}\cdot\mathbf{B}$, where $\mathbf{E}$ and $\mathbf{B}$ are the electric and magnetic fields, respectively. The term $\mathbf{E}\cdot\mathbf{B}$ is proportional to the rate of magnetic helicity production. The presence of such a term is common to many scenarios of helical magnetogenesis, including the chiral magnetic effect (CME; see Vilenkin 1980; Joyce & Shaposhnikov 1997; Boyarsky et al. 2012, 2015) and axion inflation (Barnaby et al. 2011; Turner & Widrow 1988; Fujita et al. 2015; Ng et al. 2015; Adshead et al. 2016; Cheng et al. 2016; Domcke & Mukaida 2018; Domcke et al. 2020). In the case of magnetogenesis via axion inflation (Garretson et al. 1992; Adshead et al. 2016), the helical term takes the form $f_{\rm m}^{-1}\phi F_{\mu\nu}\tilde{F}^{\mu\nu}$, where ϕ represents the axion field and $f_{\rm m}$ is a mass scale associated with the axion field. In our model, $f(a)$ is constructed such that the model avoids the aforementioned difficulties discussed in detail by Sharma et al. (2017) and SSS.

As in BS, we employ the Pencil Code (Pencil Code Collaboration et al. 2021) and apply it in two separate steps. In step I, we solve the Maxwell and GW equations near the end of the post-inflationary matter-dominated phase when the medium is still electrically nonconducting and no fluid motions can be driven by the Lorentz force. Just like the (linearized) GW equation, the Maxwell equations are linear and are advanced analytically between two subsequent times steps; see Appendix C of BS for details. In step II, when the conductivity has become large, we solve the standard magnetohydrodynamic (MHD) equations. The GW energy is always small compared with the radiation energy density and the EM energy density, which justifies the use of the linearized GW equation and the neglect of feedback onto the EM field.

The presence of the helical term proportional to γ leads to a difference in the growth rates between positively and negatively polarized fields. Magnetic fields with one of the two signs of helicities will therefore grow much faster than the other. Since there is enough time for the magnetic field to grow over many orders of magnitude, it suffices to consider in step I only fields of one helicity. This simplifies the computation somewhat. In step II, however, no such simplification is made.

In this paper, we work with conformal time η, which is related to physical time t through $\eta=\int{\rm d}t/a(t)$. By adopting appropriately scaled variables, we arrive at MHD equations that are similar to those of standard MHD for a non-expanding Universe (Brandenburg et al. 1996). In step I, during the post-inflationary matter-dominated era, the effective equation of state is such that the scale factor increases quadratically with conformal time (and like $t^{2/3}$ with physical time). Conformal time is normalized such that it is unity at the beginning of the subsequent radiation-dominated era. Furthermore, the scale factor increases linearly with η in the radiation-dominated era. We assume a spatially flat Universe and adopt the normalization of Roper Pol et al. (2020a,b), where $a(\eta)=1$ at $\eta=1$ and the mean radiative energy density is then also set to unity.

In Section 2, we present the basic equations applied in steps I and II. Those for step II are identical to the corresponding ones used in BS, but the equations for step I are different owing to the presence of the magnetic helicity producing term proportional to γ. We then present the results in Section 3 and conclude in Section 4. We adopt the Heaviside-Lorentz unit system and set the speed of light equal to unity.

2. THE MODEL

2.1. *Polarization basis and governing equations*

Any vector field can be decomposed into an irrotational and two vortical parts that are eigenfunctions of the curl operator with positive and negative eigenvalues. Here we employ the vector potential $\mathbf{A}$ in the Coulomb gauge, $\nabla\cdot\mathbf{A}=0$, so the irrotational part vanishes. We then consider $\tilde{\mathbf{A}}(\eta,\mathbf{k})=\int\mathbf{A}(\eta,\mathbf{x})\,e^{-\mathrm{i}\mathbf{k}\cdot\mathbf{x}}\mathrm{d}^3\mathbf{x}$ in Fourier space, indicated by tildae, as a function of conformal time η and the wavevector $\mathbf{k}$, and write it as

$$\tilde{\mathbf{A}}(\eta,\mathbf{k})=\tilde{A}_+(\eta,\mathbf{k})\,\tilde{\mathbf{e}}_+(\mathbf{k})+\tilde{A}_-(\eta,\mathbf{k})\,\tilde{\mathbf{e}}_-(\mathbf{k}), \quad (1)$$

where

$$\tilde{\mathbf{e}}_\pm(\mathbf{k})=[\tilde{\mathbf{e}}_1(\mathbf{k})\pm\mathrm{i}\tilde{\mathbf{e}}_2(\mathbf{k})]/\sqrt{2}\,\mathrm{i} \quad (2)$$

is the polarization basis with $\mathrm{i}\mathbf{k}\times\tilde{\mathbf{e}}_\pm=\pm k\tilde{\mathbf{e}}_\pm$, $k=|\mathbf{k}|$ is the wavenumber and $\tilde{\mathbf{e}}_1(\mathbf{k})$, $\tilde{\mathbf{e}}_2(\mathbf{k})$ represent units vectors orthogonal to $\mathbf{k}$ and orthogonal to each other. We assume an additional helical term in the EM Lagrangian density, $f^2F_{\mu\nu}(F^{\mu\nu}+\gamma\tilde{F}^{\mu\nu})$. As in BS, we assume

$$f(a)=a^{-\beta}\quad\text{with}\quad a=(\eta+1)^2/4 \quad (3)$$

being the scale factor during the post-inflationary matter-dominated era with $-1<\eta\leq 1$. The evolution of the scaled vector potential, $\tilde{\mathcal{A}}_\pm\equiv f\tilde{A}_\pm$, is then governed by the equation (SSS; Okano & Fujita 2021)

$$\tilde{\mathcal{A}}_\pm''+\left(k^2\pm 2\gamma k\frac{f'}{f}-\frac{f''}{f}\right)\tilde{\mathcal{A}}_\pm=0, \quad (4)$$

where primes denote η derivatives, and

$$\frac{f'}{f}=-\frac{2\beta}{\eta+1},\quad \frac{f''}{f}=\frac{2\beta(2\beta+1)}{(\eta+1)^2}. \quad (5)$$

There are growing modes for $k<k_*(\eta)$, given by

$$k_*(\eta)=2\beta\left(\gamma+\sqrt{1+\gamma^2+1/2\beta}\right)/(\eta+1), \quad (6)$$

where we have considered the upper sign in Equation (4). Equation (6) reduces to the expression given in Equation (7) of BS for $\gamma=0$. For $\gamma=1$, we have $k_*(1)=\beta\,(1+\sqrt{2+1/2\beta})$. For $\beta=7.3$, a particular case considered by BS, we have $k_*(1)\approx 18$ in the helical case when $\gamma=1$, which is more than twice the value $k_*(1)\approx 7.5$ for $\gamma=0$ used by BS for the nonhelical case. This shows that helicity broadens the range of unstable wavenumbers. For $\gamma=-1$, we would have $k_*(1)\approx 3.2$, but this is not relevant in practice because the fastest growing mode would then have opposite magnetic helicity, and the results for $\gamma=1$ apply analogously. Contrary to the case of nonhelical magnetogenesis ($\gamma=0$), where the growth is fastest for $k=0$, it is now fastest for finite values of k. In fact, as a function of k, the expression in round brackets in Equation (4) has an extremum for $k=2\beta\gamma/(\eta+1)$, and would instead be at $k=0$ for $\gamma=0$.

As in BS, we also solve the linearized GW equations

$$\tilde{h}_{+/\times}''+\left(k^2-\frac{a''}{a}\right)\tilde{h}_{+/\times}=\frac{6}{a}\tilde{T}_{+/\times} \quad (7)$$

for the two polarization modes of the Fourier-transformed strain $\tilde{h}_{+/\times}$. As in Roper Pol et al. (2020a,b), we have made use of the fact that the critical energy density at $\eta=1$ is unity. The GWs are driven by the $+$ and $\times$ modes of the traceless-transverse projected EM stress,

$$\mathsf{T}_{ij}=f^2\,(B_iB_j+E_iE_j), \quad (8)$$

where $\mathbf{E}=-\partial\mathbf{A}/\partial\eta$ and $\mathbf{B}=\nabla\times\mathbf{A}$ are the electric and magnetic fields in real space. We then compute $\tilde{\mathsf{T}}_{ij}(\eta,\mathbf{k})=\int\mathsf{T}_{ij}(\eta,\mathbf{x})\,e^{-\mathrm{i}\mathbf{k}\cdot\mathbf{x}}\mathrm{d}^3\mathbf{x}$ in Fourier space, project out the transverse-traceless part, and decompose the result into $\tilde{T}_+$ and $\tilde{T}_\times$, which then enter in Equation (7); see Roper Pol et al. (2020a,b) for details.

As already explained in BS, and alluded to in the introduction, we solve Equations (4) and (7) analytically between subsequent time steps. Since these equations are second order in time, the solutions to both equations are at each moment characterized by a pair of variables $(\tilde{\mathcal{A}}_\pm,\tilde{\mathcal{A}}_\pm')$ and $(\tilde{h}_{+/\times},\tilde{h}_{+/\times}')$, respectively. This implies that both the electric field and the time derivative of the strain field are readily available for computing electric and GW energies and energy spectra.

In step II, we solve the standard MHD equations with the usual modifications for a radiation-dominated ultrarelativistic gas; see also BS. The bulk motions with velocity $\mathbf{u}$ are nonrelativistic, but include second order terms in the Lorentz factor (see Brandenburg et al. 1996, 2017, for details). As stated before, the mean radiation energy density is set to unity at $\eta=1$. The new parameters in this step are the electric conductivity σ and the kinematic viscosity ν. As in BS, we always assume the magnetic Prandtl number to be unity, i.e., $\nu\sigma=1$.

2.2. *Diagnostics and initial conditions*

Important output diagnostics are energy spectra, $E_\lambda(\eta, k)$, where λ = E, M, K, and GW, for electric, magnetic, kinetic, and GW energy spectra. The symbols for the spectra are only used with these four subscripts and are not to be confused with the components of the electric field vector $\mathbf{E}$. The corresponding energy densities are given by the k integrals over these spectra, i.e., $\mathcal{E}_\lambda(\eta) = \int E_\lambda(\eta, k)\,\mathrm{d}k$. The spectra are normalized such that $\mathcal{E}_\mathrm{E} = \langle \mathbf{E}^2 \rangle/2$, $\mathcal{E}_\mathrm{M} = \langle \mathbf{B}^2 \rangle/2$, $\mathcal{E}_\mathrm{K} = \langle \mathbf{u}^2 \rangle/2$, $\mathcal{E}_\mathrm{GW} = \langle h_+'^2 + h_\times'^2 \rangle/6$.

We emphasize that $E_\mathrm{GW}(k)$ denotes the GW energy density per linear wavenumber interval, normalized to the radiation energy density at $\eta = 1$. To obtain the GW energy density per logarithmic wavenumber interval, normalized to the critical energy density today, one has to multiply $kE_\mathrm{GW}(k)$ by the dilution factor $(a_\mathrm{r}/a_0)^4 (H_\mathrm{r}/H_0)^2$, where the subscripts 'r' and '0' refer to the scale factor a and the Hubble parameter H at the end of reheating and today; see Roper Pol et al. (2020b) for details regarding the normalization. This leads to the quantity $h_0^2 \Omega_\mathrm{GW}(k) = 1.6 \times 10^{-5}\,(g_\mathrm{r}/100)\,kE_\mathrm{GW}(k)$, where g_r is the number of relativistic degrees of freedom at the beginning of the radiation dominated era.

The simulations usually start at the initial time $\eta_\mathrm{ini} = -0.9$, which implies $a(\eta_\mathrm{ini}) = 2.5 \times 10^{-3}$. In some cases (Runs C and D below), we used $\eta_\mathrm{ini} = -0.99$, so that $a(\eta_\mathrm{ini}) = 2.5 \times 10^{-5}$. As discussed in BS, the initial magnetic field usually has a spectrum $E_\mathrm{M}(k) \propto k^3$ for $k < k_*(\eta_\mathrm{ini})$. The value of $k_*(\eta_\mathrm{ini})$ lies then between the smallest and largest wavenumbers in the computational domain, k_1 and k_Ny, respectively, where $k_\mathrm{Ny} = k_1 n_\mathrm{mesh}/2$ is the Nyquist wavenumber and n_mesh is the number of mesh points in the domain of size $2\pi/k_1$. In this paper, we use $n_\mathrm{mesh} = 512$ and we treat k_1 as an input parameter that is usually chosen to be unity, but sometimes we also consider smaller and larger values between 0.2 and 10, respectively.

The transition from step I to step II is discontinuous, as was already discussed in BS. This may be permissible when the change from zero conductivity to a finite and large value occurs rapidly; see Appendix D of BS. In addition, while in step II we have $f = 1$, and therefore $f' = f'' = 0$, the values of f'/f and f''/f at the end of step I are small, but finite, which can cause artifacts. BS noted the occurrence of oscillations shortly after transitioning to step II, but the results presented for our GW spectra are always averaged over the statistically steady state and are therefore independent of the oscillations caused by the discontinuities of these two ratios. In the present case of helical magnetogenesis, there is also another effect on the spectral slope of the GW energy density that will be addressed below.

Let us emphasize at this point that in step II, when σ is large, magnetic helicity, $\langle \mathbf{A} \cdot \mathbf{B} \rangle$, is well conserved. This is not the case in step I, which is the reason why a helical magnetic field can be produced. Indeed, the magnetic helicity then grows at the same rate as the magnetic energy.

2.3. *Parameters of the magnetogenesis model*

To avoid back-reaction and strong coupling problems of magnetogenesis during inflation, SSS assumed the function f to grow in a particular fashion. In the beginning, it grows as a^α, starting from the value unity. To recover the standard EM theory at the end of reheating, f is further assumed to continue evolving as $f \propto a^{-\beta}$ in the post-inflationary era, which is assumed to be matter dominated. The procedure to obtain the value of β for a particular value of the reheating temperature T_r is the same as explained in Appendix A of BS. The only difference lies in Equation (A1) of BS, which is obtained by demanding that the total EM energy density is a certain fraction $\mathcal{E}_\mathrm{EM}$ of the background energy density at the end of the post-inflationary matter-dominated era. Details are given in Appendix A.

In the model of SSS, $\alpha = 2$ was chosen to have a scale-invariant magnetic energy spectrum during inflation. However, in the post-inflationary era, when f decreases, the part that provides a scale-invariant spectrum during inflation decays and the next order term becomes dominant, giving an $E_\mathrm{M} \propto k^3$ spectrum in the superhorizon limit. In this case, when $\alpha = 2$, the maximum possible value of the reheating temperature is approximately 50 GeV. This value is different from the value given by SSS, which was 4000 GeV. This difference is due to the fact that in SSS, the extra amplification due to the presence of the helical term was not considered in the post-inflationary matter-dominated era.

In BS, we focussed on two sets of runs—one for a reheating temperature of around 100 GeV and another for 150 MeV. The corresponding values of β where then 7.3 and 2.7, respectively. We begin with similar choices of β here, too. It turns out that for 150 MeV, the appropriate value is now $\beta = 2.9$, but for the standard scenario with $\alpha = 2$, for the reasons explained above, models for 100 GeV would not be allowed in the helical case, because they would lead to strong backreaction, which forces us to choose ≈ 10 GeV instead. In that case, the appropriate value would be $\beta = 7.7$; see Table 1 for a summary of parameter combinations and Appendix A for further details. To facilitate comparison with BS, we have reduced the value of T_r to 8 GeV, which then corresponds to $\beta = 7.3$.

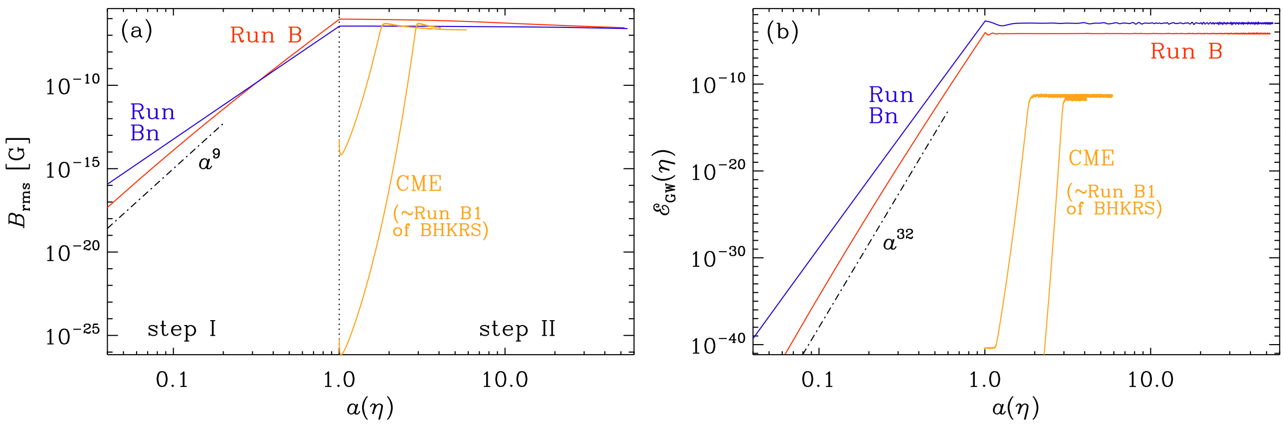

Figure 1. Evolution of (a) $B_{\rm rms}$ and (b) $\mathcal{E}_{\rm GW}$ for Runs B (with helicity, red lines) and Bn (without helicity, blue lines), both with $\beta = 7.3$, compared with two versions of Run B1 of BHKRS with CME and different initial field strengths. The two orange lines denote Run B1 of BHKRS with the original and a 10^{12} times weaker initial field. Note that for the helical growth, the slopes change with $a(\eta)$, which is a consequence of the helical term.

Table 1. β for different values of $T_{\rm r}$, α, and γ.

$T_{\rm r}$ [GeV]	$\mathcal{E}_{\rm EM}$	α	β	γ	$E_{\rm M}(\eta_{\rm ini}, k)$
10	0.07	2	7.7	1	$\propto k^3$
8	0.01	2	7.3	1	$\propto k^3$
0.15	0.01	2	2.9	1	$\propto k^3$
460	0.01	-3	3	2.5	$\propto k^{-1}$
3×10^5	0.01	1	1.7	1	$\propto k^5$

In this paper, we also explore the possibility of a smaller value of α. This allows for higher reheating temperature scales without having any back-reaction problem in the post-inflation matter-dominated era. For the case $\alpha = 1$, the value of the reheating temperature is 3×10^5 GeV when the Hubble parameter during inflation is $H_{\rm f} = 10^{14}$ GeV and the total EM energy density is 1% of the background energy density at the end of reheating. These large values of $H_{\rm f}$ and $T_{\rm r}$ were not possible for the case when $\alpha = 2$. This case is listed in the last row of Table 1 along with other relevant parameters.

We also consider the model of Okano & Fujita (2021), where $f(a) \propto a^{-3}$ both during inflation and in the post-inflationary era, i.e., $\beta = 3 = -\alpha$. In their model, the product $\beta\gamma$ was found to be 7.6 so as to have maximum magnetic field strength for the case when the total EM energy density is 1% of the background energy density; see Equation (2.19) of Okano & Fujita (2021). This corresponds to $\gamma = 2.5$. In that case, the initial magnetic field had a scale-invariant spectrum proportional to k^{-1} in the superhorizon limit.

For the magnetogenesis model at energy scales before the electroweak era, there may be additional constraints from baryogenesis in the presence of helical magnetic fields around the electroweak phase transition (Kamada & Long 2016) and from isocurvature perturbations in the cosmic background radiation Kamada et al. (2021). These constraints would disfavor such models and should be revisited in future work.

Quantum fluctuations alone would not introduce a preference of one sign of helicity over the other, so therefore both $\mathcal{A}_+$ and $\mathcal{A}_-$ would grow at the same rate if $\gamma = 0$. However, if the magnetic field was fully helical to begin with, only one of the two signs of helicity would grow, i.e., either $\mathcal{A}_+$ or $\mathcal{A}_-$, so the field might remain helical even though $\gamma = 0$ and both solutions would still be equally unstable. In the following, we allow for such a possibility in some of our simulations.

3. RESULTS

3.1. *Growth of magnetic field and GW energy*

In Figure 1, we show the growth and subsequent decay of the root-mean square (rms) magnetic field $B_{\rm rms}$ during steps I and II, and compare with a simulation of nonhelical inflationary magnetic field generation (similar to Run B1 of BS). The pair of helical and nonhelical runs shown here are referred to as Runs B and Bn, respectively. They have $\beta = 7.3$ and correspond to reheating temperatures of 8 GeV in the helical case and 100 GeV in the nonhelical case; see Table 1 for a summary of parameter combinations. The growth is still approximately algebraic, but, as expected, it is now faster than in the nonhelical case. This is caused by the extra amplification resulting from the helical term proportional to γ. This term is reminiscent of the CME, which causes, however, exponential magnetic field amplification (Joyce & Shaposhnikov 1997). The CME has

Table 2. Summary of simulation parameters and properties.

Run	T_r [GeV]	B_0	β	γ	$k_*^{(1)}$	ν	$\mathcal{E}_\mathrm{M}$	$\mathcal{E}_\mathrm{EM}$	$\mathcal{E}_\mathrm{M}/\mathcal{E}_\mathrm{EM}$	$\mathcal{E}_\mathrm{GW}$	h_rms	q_M	q_EM
A	0.15	5×10^{-10}	2.9	1	7.2	1×10^{-4}	0.012	0.023	0.51	1.2×10^{-5}	9.1×10^{-3}	2.1	1.07
B	10	4×10^{-24}	7.3	1	17	2×10^{-4}	0.050	0.11	0.48	6.6×10^{-5}	3.6×10^{-3}	2.9	1.37
Bn	10	3×10^{-18}	7.3	0	7.5	2×10^{-4}	0.007	0.19	0.04	1.0×10^{-3}	2.4×10^{-2}	32	1.30
C	460	1×10^{-27}	3.0	2.5	15	1×10^{-4}	0.014	0.017	0.80	1.6×10^{-6}	8.1×10^{-4}	1.4	1.14
D	3×10^{5}	5×10^{-6}	1.7	1	4.3	5×10^{-4}	0.016	0.025	0.64	8.5×10^{-5}	7.6×10^{-3}	2.5	1.58
Dn	3×10^{5}	1×10^{-3}	1.7	0	1.9	2×10^{-4}	0.016	0.052	0.30	2.8×10^{-3}	5.7×10^{-2}	6.6	1.98

been invoked in the study of GW production from the resulting magnetic field both analytically (Anand et al. 2019) and numerically (Brandenburg et al. 2021c, hereafter BHKRS). The difference in the temporal growth of B_rms and $\mathcal{E}_\mathrm{GW}$ between the CME and helical magnetogenesis is demonstrated in Figure 1. Here we have also overplotted two versions of Run B1 of BHKRS. (We stress that this Run B1 is different from the Run B1 of BS.)

During the subsequent decay phase, B_rms is approximately equally large for both inflationary and CME runs. This is just because of our choice of parameters. However, owing to the smaller length scales on which the CME operates, the corresponding GW energy is now much smaller than for inflationary magnetogenesis. On the other hand, we also see that the growth, being exponential, is much faster for the CME runs than for both the helical and nonhelical inflationary magnetogenesis models. This implies that the CME can reach saturation with an arbitrarily weak initial seed magnetic field. The saturation amplitude does, however, depend on the assumed initial imbalance of left- and right-handed fermions, and may, in reality, be much smaller than what has been assumed in the models of BHKRS. By contrast, the maximum field strength from inflationary magnetogenesis is determined by demanding that the total EM energy density is some fraction of the background energy density at the end of reheating so that there is no back-reaction.

In Table 2, we summarize quantitative aspects of our new runs, Runs A–D, as well as two nonhelical ones, Runs Bn and Dn, where $\gamma=0$. We list the reheating temperature T_r in GeV, the amplitude parameter B_0 for the initial magnetic field, the aforementioned parameters β, γ, $k_*^{(1)}$, and ν, as well as the output parameters $\mathcal{E}_\mathrm{M}$, $\mathcal{E}_\mathrm{EM}\equiv\mathcal{E}_\mathrm{E}+\mathcal{E}_\mathrm{M}$, the ratio $\mathcal{E}_\mathrm{M}/\mathcal{E}_\mathrm{EM}$, the values of $\mathcal{E}_\mathrm{GW}$ and the rms strain $h_\mathrm{rms}=\langle h_+^2+h_\times^2\rangle^{1/2}$, as well as two different efficiency parameters q_M and q_EM, defined below.

As in BS, varying the initial magnetic field strength B_0 always resulted in a purely quadratic change of $\mathcal{E}_\mathrm{M}$, and a quartic change of $\mathcal{E}_\mathrm{GW}$. It therefore suffices to present, for each combination of parameters β and γ, only one value of B_0, typically such that $\mathcal{E}_\mathrm{EM}$ is roughly in the expected range of between 0.01 and 0.1.

Comparing helical with nonhelical runs for similar values of $\mathcal{E}_\mathrm{M}$, the GW energies and strains are smaller than in the earlier cases without helicity (see also Figure 1). This may suggest that GW production from helical inflationary magnetogenesis is somewhat less efficient than for the nonhelical case. However, while the values of $\mathcal{E}_\mathrm{M}$ are the same, the total EM energies, $\mathcal{E}_\mathrm{EM}=\mathcal{E}_\mathrm{E}+\mathcal{E}_\mathrm{M}$, are not. In fact, we see that the ratio $\mathcal{E}_\mathrm{E}/\mathcal{E}_\mathrm{M}$ is typically 0.3–0.5, i.e., the electric energy contribution is subdominant during the post-inflationary matter-dominated era. For nonhelical magnetogenesis, by contrast, the electric energy is dominant, typically with $\mathcal{E}_\mathrm{E}/\mathcal{E}_\mathrm{M}=10$–$30$ for β between 2.7 and 7.3.

As already noted, for fixed values of β and γ, the different values of $\mathcal{E}_\mathrm{M}$, $\mathcal{E}_\mathrm{EM}$, $\mathcal{E}_\mathrm{GW}$, and h_rms are directly related to the initial amplitude parameter B_0. To compare runs with different parameters β and γ, we must therefore compute normalized efficiencies. Earlier work (Roper Pol et al. 2020b; Brandenburg et al. 2021b) suggested that $\mathcal{E}_\mathrm{GW}=(q_\mathrm{M}\mathcal{E}_\mathrm{M}/k_\mathrm{c})^2$, where q_M is the efficiency and k_c is a characteristic wavenumber. In analogy to their work, we now postulate an analogous relation, but with $\mathcal{E}_\mathrm{EM}$ instead of $\mathcal{E}_\mathrm{M}$, i.e.,

$$\mathcal{E}_\mathrm{GW}=(q_\mathrm{EM}\mathcal{E}_\mathrm{EM}/k_\mathrm{c})^2, \tag{9}$$

where q_EM is a new efficiency parameter, and for k_c we always take the value $k_\mathrm{c}=k_*(1)$, just like in BS. We recall that in Equation (9), $\mathcal{E}_\mathrm{GW}$ and $\mathcal{E}_\mathrm{EM}$ are in units of the radiation energy density at $\eta=1$ and k_c is in units of H_r/c.

For nonhelical magnetogenesis, BS found that q_M was proportional to β. Since $k_*(1)$ was also proportional to β, this meant that the effect of dividing by $k_*(1)$ was effectively canceled, and that therefore a good scal-

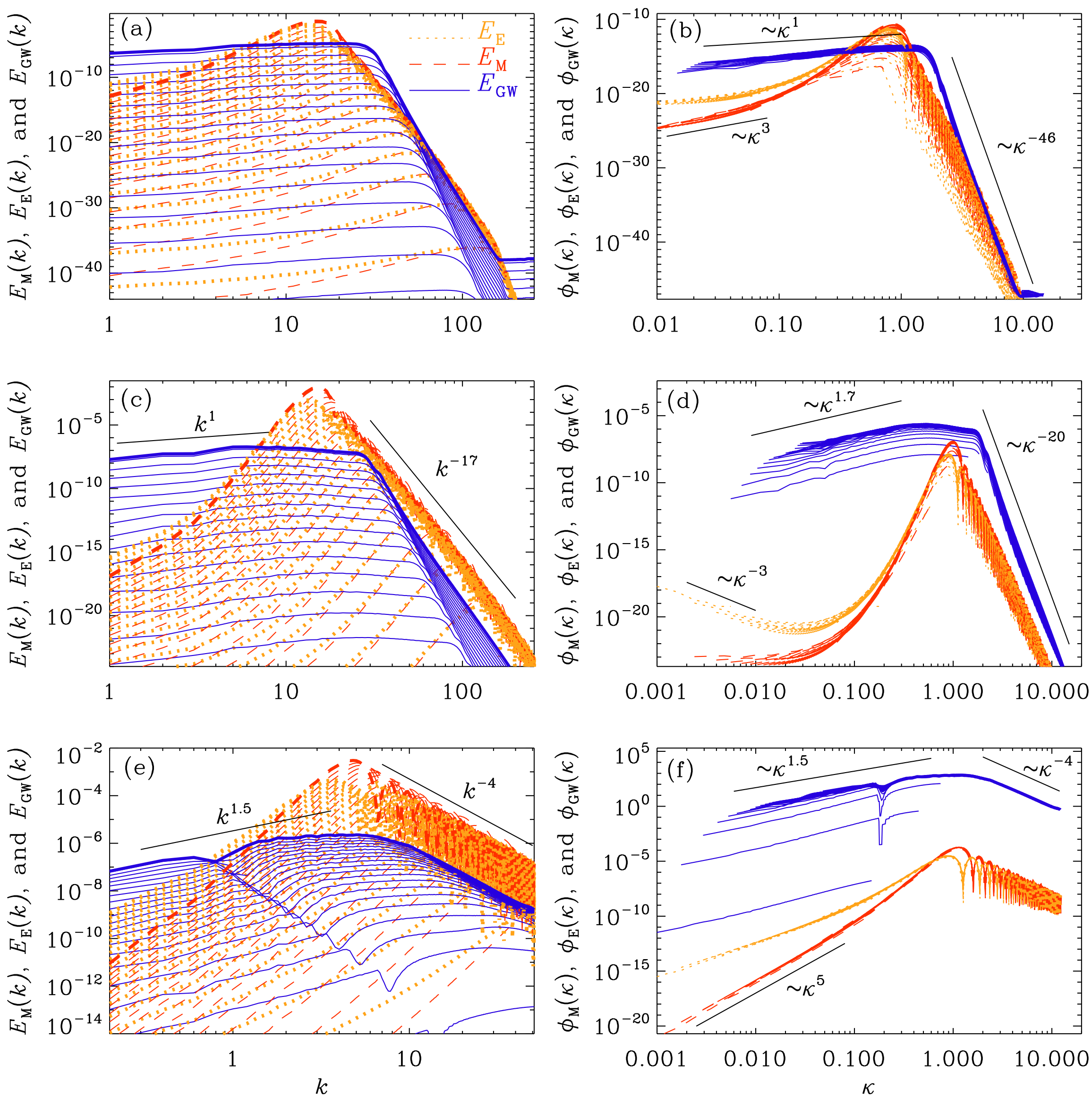

Figure 2. $E_{\rm M}(k)$ (red lines), $E_{\rm E}(k)$ (orange lines), and $E_{\rm GW}(k)$ (blue lines) for (a) Run B, (c) Run C, and (e) Run D, together with the associated collapsed spectra $\phi_{\rm M}(\kappa)$ (red lines), $\phi_{\rm E}(\kappa)$ (orange lines), and $\phi_{\rm GW}(\kappa)$ (blue lines) for (b) Run B, (d) Run C, and (f) Run D. The spectral GW energy increases at a rate that is independent of k, but the exponent characterizing the growth of $E_{\rm M}(k)$ does depend on k.

ing was obtained by just plotting $\mathcal{E}_{\rm GW}$ versus $\mathcal{E}_{\rm M}^2$, suggesting that the $1/k_{\rm c}$ scaling may not have been real. However, our new results for helical magnetogenesis now show that this is not the case for $q_{\rm EM}$. In fact, looking at Table 2, where we present both $q_{\rm M}$ and $q_{\rm EM}$, we see that $q_{\rm M}$ shows significant variations ($1.4 \lesssim q_{\rm M} \lesssim 32$), while $q_{\rm EM}$ changes comparatively little ($1 \lesssim q_{\rm EM} \lesssim 2$). This suggests that the GW energy is indeed governed by $q_{\rm EM}$, and is then only weakly dependent on the value of β.

Among the four runs A–D, Runs A and B have the same values of α and γ, their initial spectra are the same (see Table 1), and only the values of β are different. For Runs C and D, on the other hand, also the values of γ and α were different. In the following, therefore, we focus on presenting Runs B–D in more detail.

3.2. *Energy spectra*

Next, we compare Runs B, C, and D by looking at the GW and magnetic energy spectra for step I during $-0.9 \le \eta \le 1$, where we also compare with electric energy spectra. As in BS, we try to collapse the spectra on top of each other by plotting the functions

$$\phi_\lambda(\kappa) = (\eta+1)^{-(p_\lambda+1)} E_\lambda(k,\eta), \qquad (10)$$

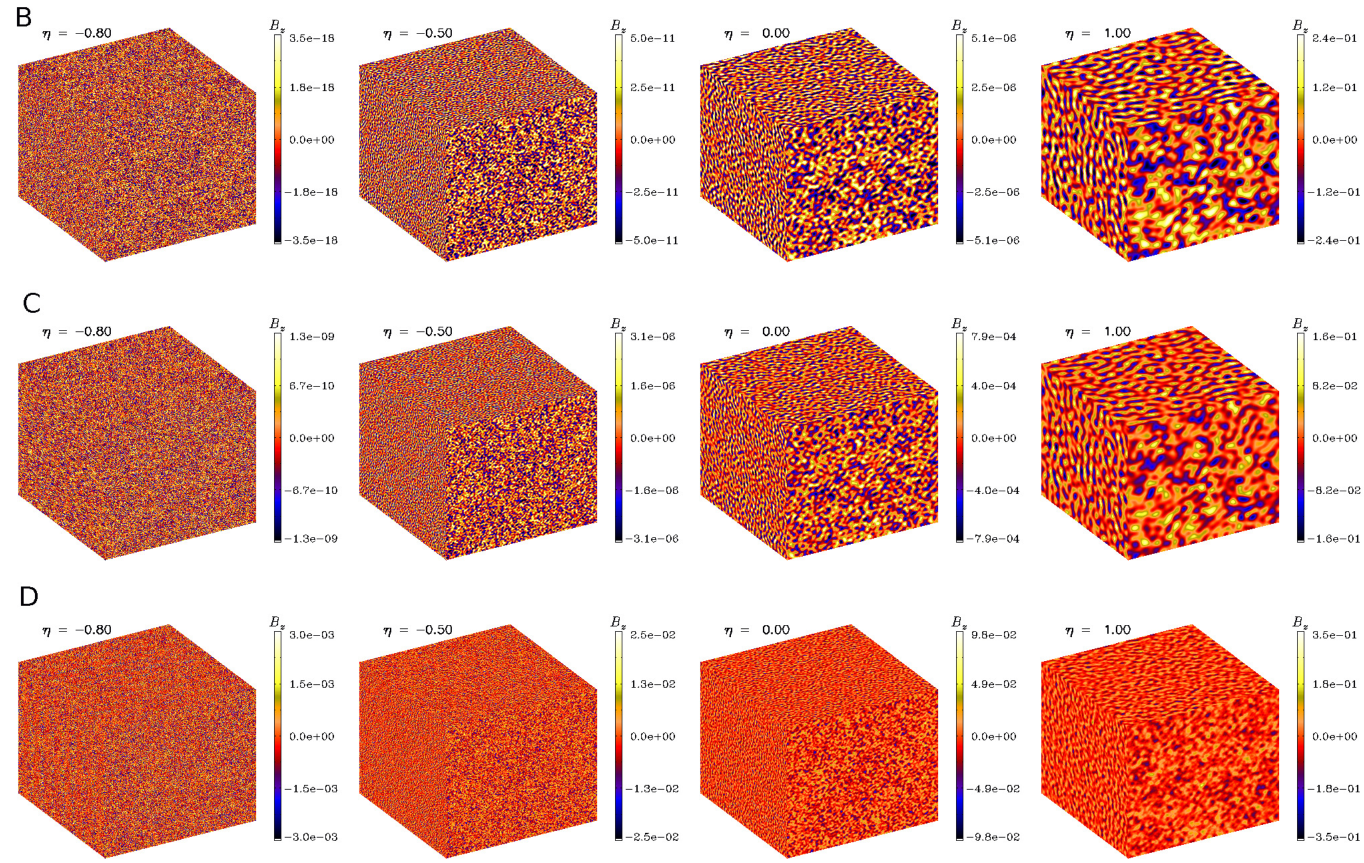

Figure 3. Visualizations of B_z for Runs B (top), C (middle), and D (bottom) on the periphery of the computational domain for $\eta = -0.8$, -0.5, 0, and 1 during step I. The color scale is symmetric about zero and adjusted with respect to the instantaneous extrema.

where $\lambda = \mathrm{E}$, M, or GW for electric, magnetic, and GW energies, respectively, p_λ are exponents characterizing the growth, and

$$\kappa(\eta) = k/k_*(\eta) \tag{11}$$

is a time-depended wavenumber where the EM energy spectra peak. We show the result in Figure 2, where we plot both $E_\lambda(k,\eta)$ and $\phi_\lambda(\kappa)$ for Run B in panels (a) and (b), Run C in panels (c) and (d), and Run D in panels (e) and (f). The values of p_λ are listed in Table 3 for Runs A–Dn. We see that the tendency of the lines to collapse on top of each other is better for the GW spectra than for the electric and magnetic spectra. This shows that those latter two are not shape-invariant. This is clearly different from the nonhelical case; see the corresponding Figure 3 of BS.

Interestingly, except for the GW spectra, which show power law scalings with $E_{\mathrm{GW}}(k) \propto k$ for $k < 2k_*(1)$ and $E_{\mathrm{GW}}(k) \propto k^{-46}$ for $k > 2k_*(1)$ (for Run B), the EM spectra deviate from power law scaling and show a more peaked spectrum for $k < k_*(1)$. The growth is fastest in the model with $\beta = 7.3$, as is indicated by the spectra spanning about forty orders of magnitude and by the large values of p_{M} and p_{GW}; see Table 3 for Run B. For Runs C and D, the spectra are progressively more shallow.

For the GW spectrum of Run D, there is a dip at $\kappa \approx 0.17$ (and at decreasing values of k as time increases). This coincides with the wavenumber where $k^2 = a''/a$ and thus, where the solution to Equation (7) changes from oscillatory to temporally growing behavior. This feature is now so prominent, because the growth of the magnetic field for Run D is much slower than for Runs B and C.

Table 3. Values of β, p_{M}, and p_{GW} for Runs A–Dn.

Run	A	B	Bn	C	D	Dn
β	2.9	7.3	7.3	3	1.7	1.7
p_{M}	12	30	28	16	4.0	3.8
p_{GW}	22	62	53	29	4.9	4.6

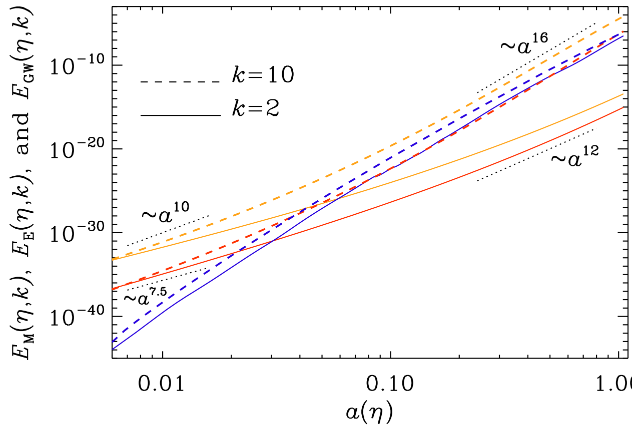

Figure 4. Temporal dependence represented through $a(\eta)$ of spectral energies at $k = 2$ (solid lines) and $k = 10$ (dashed lines) for Run C with $E_{\rm M}(\eta, k)$ (red lines), $E_{\rm E}(\eta, k)$ (orange lines), and $E_{\rm GW}(\eta, k)$ (blue lines).

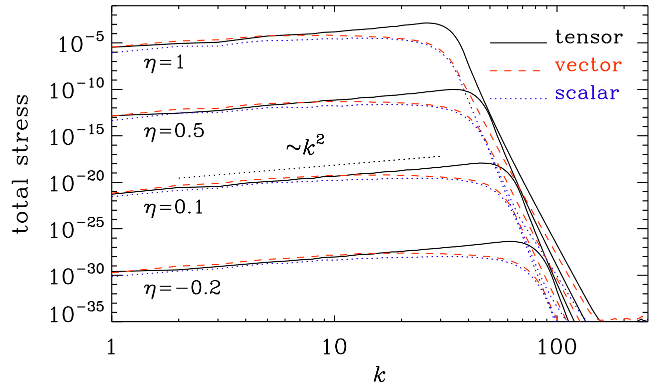

Figure 5. Spectra of the total stress at $\eta = -0.2$, 0.1, 0.5, and 1, decomposed into tensor (solid black), vector (dashed red), and scalar modes (dotted blue) for Run B of Figure 2.

Visualizations of the magnetic field on the periphery of the computational domain are shown in Figure 3 for Runs B–D. We see that the typical length scales increase with time, but again faster for Runs B and C than for Run D.

To study the temporal growth for specific values of k, we show in Figure 4 the dependencies of $E_{\rm E}(\eta, k)$, $E_{\rm M}(\eta, k)$, and $E_{\rm GW}(\eta, k)$ separately for $k = 2$ and 10 for Run C, where the departure from shape-invariant behavior appears to be the strongest. We clearly see that the growth of $E_{\rm GW}(\eta, k)$ is the same for all values of k. This is in agreement with the visual impression from Figure 2. It is also the same at early and late times. This is not the case for the electric and magnetic spectra, where we have a growth proportional to $a^{7.5}$ for $k = 2$ and small values of a, but a faster growth $\propto a^{16}$ for $k = 10$ and $a(\eta) > 0.1$.

When the mode corresponding to a certain wavenumber k is well outside the horizon, the f''/f term within the round brackets of Equation (4) dominates over the other two terms, and the amplitude of the mode grows in time. Once the mode is about to enter the horizon, the second term also comes into the picture and further enhances the growth rate for $\gamma = 1$. This behavior is shown in Figure 4.

To understand the nearly shape-invariant scaling of $E_{\rm GW}(\eta, k)$, it is important to look at spectra of the stress. This is done in Figure 5, where we show spectra of the stress, decomposed into tensor, vector, and scalar modes (Mukhanov et al. 1992). The tensor mode is the transverse-traceless contribution to the stress, while the vector and scalar modes are composed of vortical and irrotational constituents, respectively; see Brandenburg et al. (2021b) for such a decomposition of data from earlier GW simulations. We see that at all times during step I, the scalar and vector modes are subdominant. In particular the peak of the stress spectrum is, to a large fraction, composed of the tensor mode only. As expected from the work of Brandenburg & Boldyrev (2020), its spectrum follows a k^2 subrange to high precision.

Comparing the different models, we see that for $\kappa \ll 1$, we reproduce the initial scalings $\phi_{\rm M} \propto \kappa^3$ for Run B and $\propto \kappa^5$ for Run D, with a shallower scaling by a factor κ^2 for the electric fields, in particular the $\phi_{\rm E} \propto \kappa^{-3}$ scaling for Run C. For $\kappa \gg 1$, we have a progressively shallower decline $\propto \kappa^{-46}$, κ^{-20}, and κ^{-4} as we go from Run B to Runs C and D.

3.3. *Spectra in step II*

In step II, a velocity field emerges, driven by the Lorentz force. This causes the magnetic field to develop small-scale structure, as can be seen from Figure 6(a). This leads to a turbulent cascade that has here a spectrum proportional to k^{-3} for large k; see Figure 6(b). Contrary to BS, the new GW spectrum now shows a flat power law scaling for $k < 2k_*(1)$ with $E_{\rm GW}(k) \propto k^0$, i.e. $kE_{\rm GW}(k) \propto k^1$. Such a scaling was already found by Roper Pol et al. (2020b). The reason for this lies in the direct correspondence with the relevant magnetic stress for the blue-tilted magnetic energy spectrum, where $E_{\rm M}(k)$ has an increasing slope with an exponent larger than two, which corresponds to a white noise spectrum. In that case, this stress itself always has a white noise spectrum and cannot be steeper than that. This was shown by Brandenburg & Boldyrev (2020), who just considered the stress spectrum and ig-

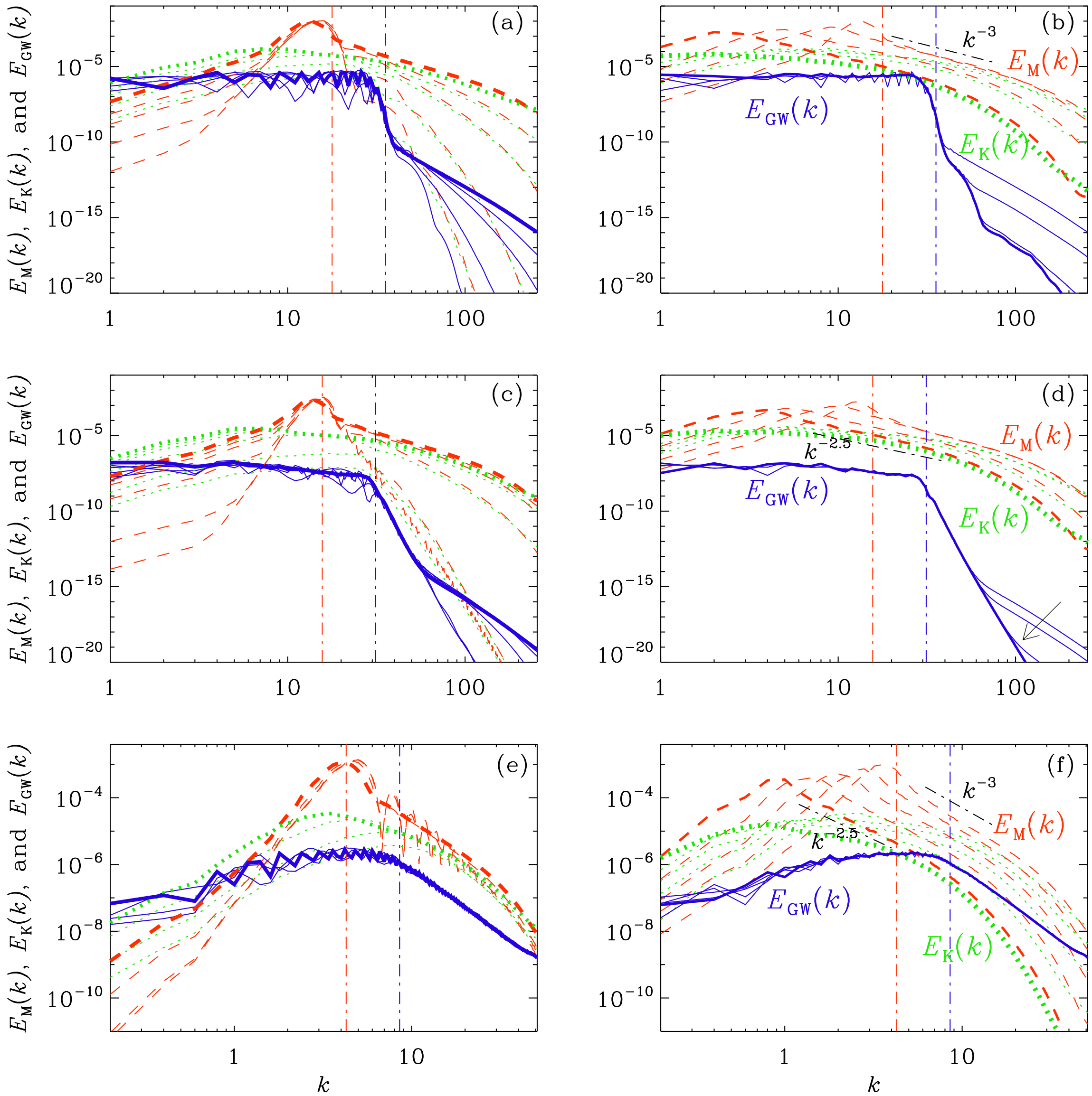

Figure 6. Early times in the beginning of the radiation-dominated phase for (a) Run B ($\eta = 1.06$, 1.2, 1.4, 1.6, and 2.1), (c) Run C ($\eta = 1.06$, 1.9, 2.7, 3.3, and 4.1), and (e) Run D ($\eta = 1.6$, 2.1, 3.6, and 6.1). $E_{\rm M}(k)$, $E_{\rm K}(k)$, and $E_{\rm GW}(k)$ are shown as dashed red, dotted green, and solid blue lines, respectively. The last times are shown as thick lines. Later times are shown separately for (b) Run B ($\eta = 2$, 6, 16, and 52), (d) Run C ($\eta = 11$, 26, and 52), and (f) Run D ($\eta = 11$, 26, 51, 101, and 213). The red and blue vertical dashed-dotted lines goes through $k_*(1)$ and $2k_*(1)$, respectively. Again, thick lines denote the last time. The arrow in panel (d) highlights the sense of time, where $E_{\rm GW}(k)$ declines at large values of k.

nored temporal aspects, i.e., they did not consider solutions to the GW equation.

As in BS, the GW spectrum shows a marked drop by about six orders of magnitude for Run B, which is slightly more than what was found in BS and also in Brandenburg et al. (2021a). We return to this in Section 3.4, but we note at this point that for $k \gg 2k_*(1)$ in Runs B and C, the spectral GW energy beyond the drop, which is very small already, becomes even smaller as time goes on. This is indicated by the arrow in Figure 6(d). Eventually, the spectrum settles at a level close to the fat blue lines in Figure 6, which marks the last time. Furthermore, at late times, Figure 6(b) shows clear inverse cascading with the peak of the magnetic spectra traveling toward smaller k; see the red dashed lines in Figure 6. The height of the peak is expected to stay unchanged (Brandenburg & Kahniashvili 2017), but our present runs show a small decline with time. This is predominantly a consequence of the conductivity still not being high enough. Larger conductivity would

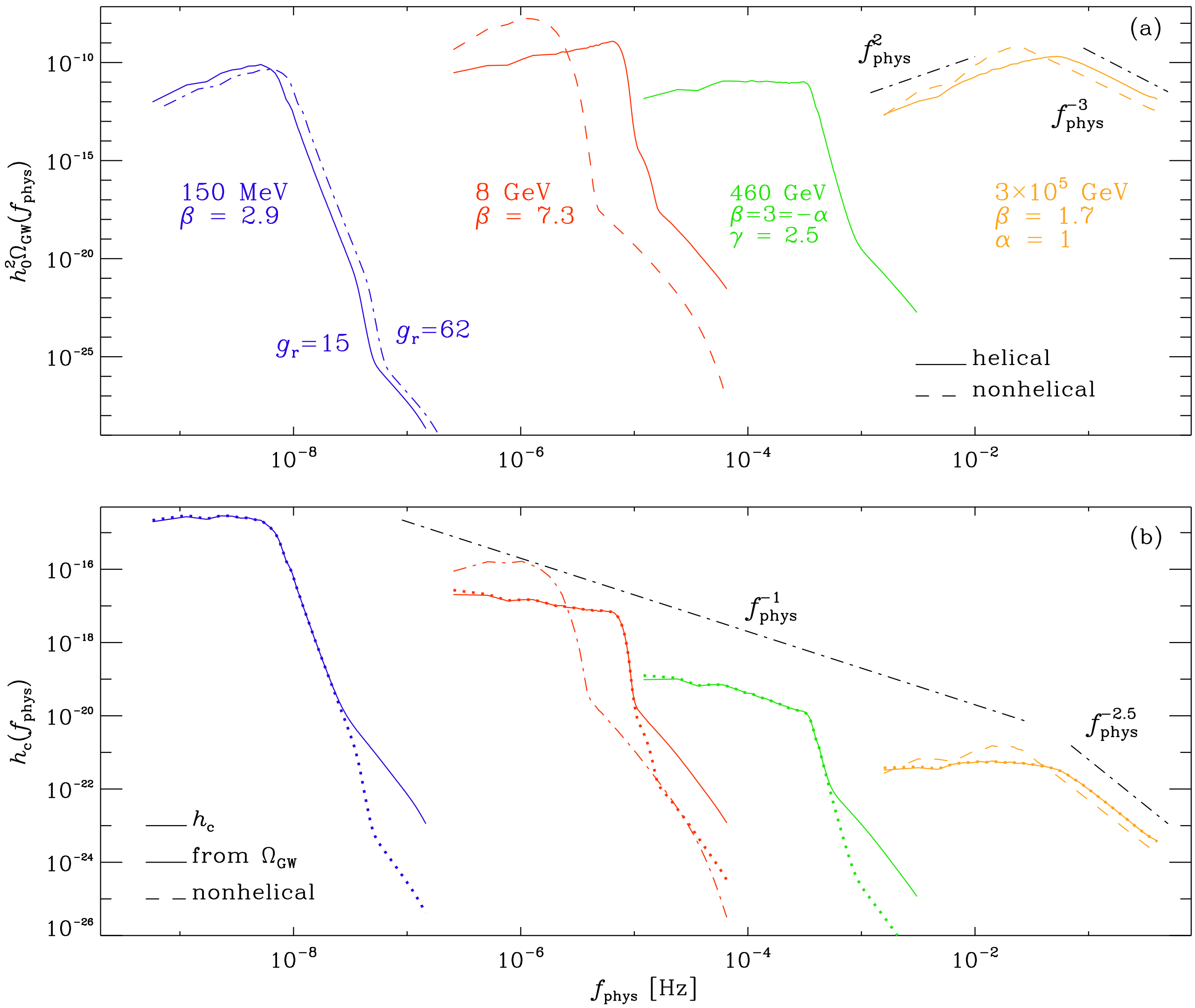

Figure 7. (a) $h_0^2\Omega_{\rm GW}(f_{\rm phys})$ and (b) $h_c(f_{\rm phys})$ for Runs A–D $T_{\rm r}$ ranging from 150 MeV to 3×10^5 GeV. In (a), dashed lines denote nonhelical runs and dashed-dotted show the result for $g_{\rm r}=62$. In (b), the dotted lines denote $1.26\times10^{-18}\sqrt{h_0^2\Omega_{\rm GW}}\,(1\,{\rm Hz}/f_{\rm phys})$ (Maggiore 2000), and are labelled as "from $\Omega_{\rm GW}$".

require larger numerical resolution, which would begin to pose computational memory problems.

In step II, the GW spectrum is now fairly flat, $E_{\rm GW}\propto k^0$ for Runs B and C, and with a slight rise $\propto k$ for Run D. Therefore, the GW energy per logarithmic wavenumber interval, normalized by the critical energy density for a spatially flat universe, is $\Omega_{\rm GW}\propto kE_{\rm GW}\propto k^1$ for Run B, and perhaps even slightly shallower for Run C, and $\propto k^2$ for Run D. Thus, as already seen in many earlier numerical simulations of turbulence-driven GWs (Roper Pol et al. 2020b, BHKRS), this is shallower than the previously expected k^3 scaling (Gogoberidze et al. 2007; Okano & Fujita 2021). In the present case, during the onset of MHD turbulence, the spectrum has changed from a k^1 spectrum to a k^0 spectrum. As explained in Appendix F of BS, this is associated with the discontinuous behavior of f'/f and f''/f. They concluded that the change from a k^1 spectrum to k^0 occurs when the growth of EM energy has stopped. This is at the same time when $f'=f''=0$, but it is not a direct consequence of the discontinuity at $\eta=1$ and therefore not an artifact.

We see clear inverse cascading in the magnetic energy spectra with the peak of the spectrum moving toward smaller k. This has been investigated in detail in many earlier papers (Hatori 1984; Biskamp & Müller 1999; Kahniashvili et al. 2013); see Brandenburg & Kahniashvili (2017) for a demonstration of the self-similarity of the magnetic energy spectra. The conservation of mean magnetic helicity density,

$\langle \mathbf{A}\cdot\mathbf{B}\rangle$, implies a growth of the correlation length and a corresponding decay of the mean magnetic energy density such that $\langle \mathbf{A}\cdot\mathbf{B}\rangle \approx \pm B_{\rm rms}^2 \xi_{\rm M} \approx$ const for fully helical turbulence, where the two signs apply to positive and negative magnetically helicities, respectively.

3.4. *Observable spectra*

In Figure 7, we show the final spectra of $\Omega_{\rm GW}$ and $h_{\rm c}$ versus temporal frequency $f_{\rm phys} = kH_{\rm r}/2\pi a_0$ for the present time. The frequency $f_{\rm phys}$ is not to be confused with the function $f(a)$, defined in Equation (3), which does not carry any subscript. In principle, such spectra should have been computed from a temporal Fourier transform. The equivalence between spatial and temporal Fourier spectra was demonstrated by He et al. (2021), who also showed that there are significant differences when the dispersion relation is modified by a finite graviton mass. However, temporal spectra tend to be more noisy owing to smaller statistics, which is why those are not used here. Both the strain and energy spectra are scaled for the corresponding values of $T_{\rm r}$ between 150 MeV and 3×10^5 GeV. We have indicated spectra for the nonhelical case as dashed lines.

The spectra in Figure 7 show different shapes of the $\Omega_{\rm GW}$ spectra for helical and nonhelical runs. This may, to some extent, be caused by the larger values of $k_*(1)$ in these helical runs. The drop beyond the peak is here actually weaker than in the nonhelical case. This was different from what was found in previous simulations (Roper Pol et al. 2020b; Brandenburg et al. 2021a), and may be related to the presence of a weaker forward cascade in favor of a stronger inverse cascade in helical turbulence (Pouquet et al. 1976). Note also that for Run B with the largest value of β, the change from the scaling $\Omega_{\rm GW} \propto f_{\rm phys}$ is much sharper in the case with helicity than without, where the spectra are much rounder.

In the model with $T_{\rm r} = 150$ MeV, we compare the GW spectra generated both before and after the QCD phase transition, where $g_{\rm r}$ changes by a factor of about four from 62 to about 15. This leads to a decrease in frequency by a factor $\propto g_{\rm r}^{1/2}$ of about two, and an increase in GW energy by a factor $\propto g_{\rm r}^{1/3}$ of about 1.6.

We see that the high $T_{\rm r}$ model is different from the other models with lower $T_{\rm r}$ in several respects. The drop in GW energy above the maximum is now absent and the inertial range slope is no longer $\propto f_{\rm phys}$, but $\propto f_{\rm phys}^2$. This is mainly caused by the small value of β, which results in a slower growth. At the same time, the spectral peak at $k_*(\eta)$ still moves to smaller values, as before. This causes the slope for $k > 2k_*(1)$ to be shallower than in the other models with larger values of β. The slope is then also inherited in step II, and it is then not much affected any more by the emerging turbulence.

The model of Okano & Fujita (2021) with $T_{\rm r} = 460$ GeV corresponds to our Run D. They also studied GW production, but they did not include the turbulent phase after reheating. Comparing our Figure 7 with Figure 5 of Okano & Fujita (2021), we see that the peak values are slightly different. Our spectral peak is at approximately $h_0^2\Omega_{\rm GW} \approx 10^{-11}$, while their peak value without the h_0^2 factor is $\Omega_{\rm GW} \approx 10^{-12}$. Furthermore, as we saw already from Figure 6, the slope of $E_{\rm GW}(k)$ was slightly negative close to the peak. Therefore, the $\Omega_{\rm GW}(k) \propto kE_{\rm GW}(k)$ is now nearly flat. This is quite different from Figure 5 of Okano & Fujita (2021), which had a clear $\Omega_{\rm GW}(k) \propto k^3$ range below the peak. The frequency corresponding to the peak is also slightly different, but this is to some extent explained by their frequency lacking a 2π factor.

3.5. *Circular polarization*

In Figure 8(a), we plot the time-averaged fractional circular polarization spectrum of GWs, $\mathcal{P}_{\rm GW}(k)$, for Run B. It is defined as (see Equation B.17 of Roper Pol et al. 2020a)

$$\mathcal{P}_{\rm GW}(k) = \int 2\,{\rm Im}\,\tilde{h}_+\tilde{h}_\times^*\,k^2{\rm d}\Omega_k \Big/ \int \left(|\tilde{h}_+|^2 + \tilde{h}_\times|^2\right) k^2{\rm d}\Omega_k. \tag{12}$$

In Figure 8(b), we show the fractional magnetic helicity spectrum,

$$\mathcal{P}_{\rm M}(k) = kH_{\rm M}(k)/2E_{\rm M}(k), \tag{13}$$

where $H_{\rm M}(k)$ is the magnetic helicity spectrum, normalized such that $\int H_{\rm M}(k)\,{\rm d}k = \langle \mathbf{A}\cdot\mathbf{B}\rangle$. Unlike the GW spectrum, which is statistically stationary and we can take a long-term average, the magnetic field develops a forward cascade and decays at the same time. During that time, the kinetic energy density has a maximum, which marks the moment when the turbulent cascade has developed. We have therefore decided to take a short-term average of the magnetic helicity and energy spectra around the time when the kinetic energy density is within about 70% of its maximum value.

We also compare with the corresponding spectrum from Run B1 of BHKRS with CME (not to be confused with Run B1 of BS). Except for a hundredfold shift toward larger k, the shapes of $\mathcal{P}_{\rm GW}(k)$ are similar in that both have a plateau with $\mathcal{P}_{\rm GW}(k) \approx 1$ and a similar decline toward smaller values of k.

Toward larger values of k, we see a drop in $\mathcal{P}_{\rm GW}(k)$ that is superficially similar to the drop in GW energy—at least for the present runs. In the runs driven by the

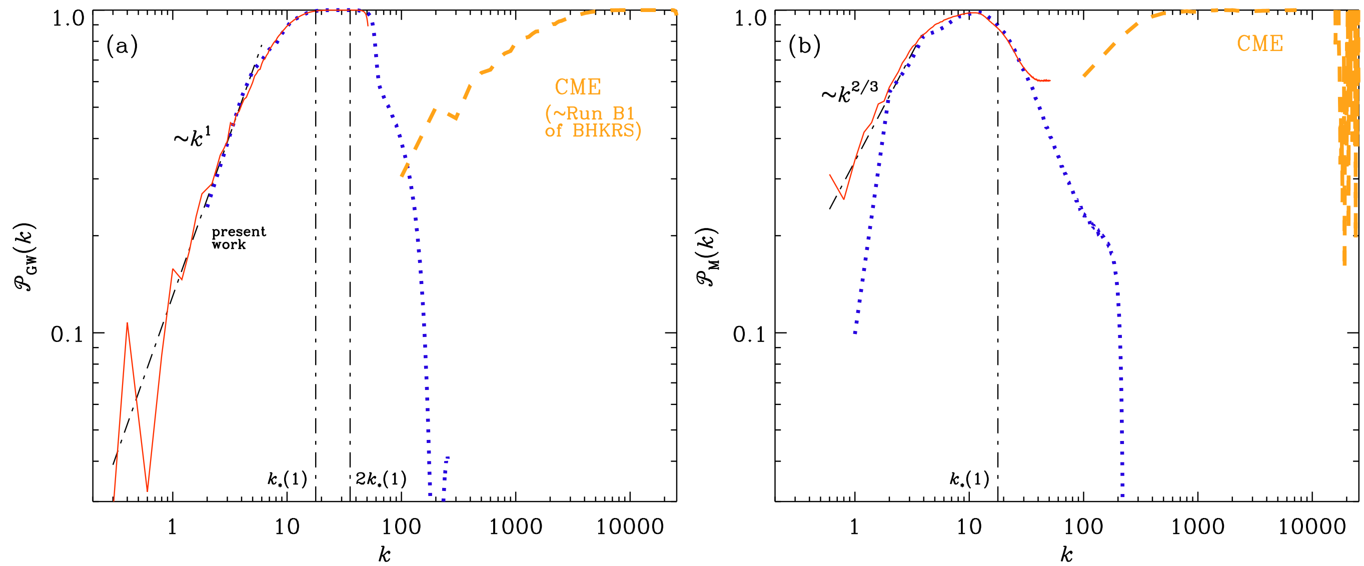

Figure 8. (a) $\mathcal{P}_{\rm GW}(k)$ and (b) $\mathcal{P}_{\rm M}(k)$ for Run B (with $k_1=1$; blue dotted lines) and a corresponding run with $k_1=0.2$ (red solid lines), as well as for Run B1 of BHKRS (orange dashed line). The vertical dashed-dotted lines mark the positions of $k_*(1)$ in (a) and (b) and of $2k_*(1)$ in (a).

CME, such a drop is absent. However, the drop in the GW energy spectra for large k is probably not related to the drop seen in the polarization spectra, where it appears for a larger k value of nearly $4k_*(1)$. Furthermore, at about $k=k_*(1)$, we rather see that $\mathcal{P}_{\rm GW}(k)$ declines toward *smaller* k values, i.e., for $k<2k_*(1)$.

We have confirmed that the decline below $k=k_*(1)$ is not related to the finite domain size. We have also performed a simulation with a five times larger domain, where $k_1=0.2$ instead of $k_1=1$. By comparing these two runs, we recovered essentially the same $\mathcal{P}_{\rm GW}(k)$ profile. This is shown in Figure 8 as the red solid line, which agrees with the blue dotted one for not too small k values. In particular, we see that there is evidence for a linear scaling of the fractional polarization, i.e., $\mathcal{P}_{\rm GW}(k)\propto k$.

Comparing with the fractional magnetic helicity spectrum, $\mathcal{P}_{\rm M}(k)$, we see that it also declines toward smaller k, but this happens more slowly. In fact, for Run B, where $\mathcal{P}_{\rm GW}(k)$ already declines, $\mathcal{P}_{\rm M}(k)$ is just reaching its maximum. For larger values of k, we see that $\mathcal{P}_{\rm M}(k)$ already declines for Run B while $\mathcal{P}_{\rm GW}(k)$ is still at its plateau. However, for the CME runs, no decline in $\mathcal{P}_{\rm M}(k)$ is seen.

3.6. *Present day values*

The values of $\mathcal{E}_{\rm M}$ listed in Table 2 gave the magnetic energy fraction of the radiation energy at $\eta=1$. To obtain the comoving rms magnetic field in gauss, we set $B_{\rm rms}^2/8\pi=\mathcal{E}_{\rm M}\,(\pi^2 g_0/30)\,(k_{\rm B}T_0)^4/(\hbar c)^3$, where $g_0=3.38$ and $T_0=2.7\,{\rm K}$ is the present day temperature, $k_{\rm B}$ is the Boltzmann constant, and $\hbar$ is the reduced Planck constant. By using $\mathcal{E}_{\rm EM}=0.01$ in all cases, we can compute $\mathcal{E}_{\rm M}$ by taking the $\mathcal{E}_{\rm M}/\mathcal{E}_{\rm EM}$ ratios from Table 2 for Runs A–D. Likewise, we use Equation (9) with the $q_{\rm EM}$ values listed in that table and compute $h_0^2\Omega_{\rm GW}$ from $\mathcal{E}_{\rm GW}$ by multiplying with the appropriate dilution factor.

At $\eta=1$, the typical magnetic correlation length is taken to be $\xi_{\rm M}=c/H_{\rm r}k_*(1)$. To compute the present values, we assume turbulent inverse cascading at constant magnetic helicity until the matter-radiation equality using $B_{\rm rms}^{\rm eq}=B_{\rm rms}^{\rm r}\eta_{\rm eq}^{-1/3}$ and $\xi_{\rm M}^{\rm eq}=\xi_{\rm M}^{\rm r}\eta_{\rm eq}^{2/3}$, where $\xi_{\rm M}^{\rm r}=(a_0/a_{\rm r})\,\xi_{\rm M}$ and superscripts 'r' and 'eq' indicate comoving values at reheating and matter–radiation equality, respectively. The value of $\eta_{\rm eq}$ is obtained by using $g_{\rm eq}^{1/3}a_{\rm eq}T_{\rm eq}=g_{\rm r}^{1/3}a_{\rm r}T_{\rm r}$, implied by the adiabatic evolution of the Universe and $a_{\rm eq}=\eta_{\rm eq}$, where we take $T_{\rm eq}=1{\rm eV}$ and $g_{\rm eq}=3.94$. The results are listed in Table 4.

We emphasize here that, unlike the magnetic field, which can have much larger length scales owing to inverse cascading (Pouquet et al. 1976), this is not the case for GWs. This is because GWs are governed by the imprint from the time when the stress was maximum.

4. CONCLUSIONS

The present work has demonstrated that helical inflationary magnetogenesis modifies the nonhelical case in such a way that the electric and magnetic power spectra become strongly peaked at a finite wavenumber, corresponding typically to about a tenth of the horizon scale at $\eta=1$. Such a distinct wavenumber does not exist

Table 4. Present day values for Runs A–D using parameters from Table 2 as input, assuming always $\mathcal{E}_{\rm EM}=0.01$.

Run	$T_{\rm r}$ [GeV]	$\eta_{\rm eq}$	$\xi_{\rm M}^{\rm r}$ [Mpc]	$\xi_{\rm M}^{\rm eq}$ [Mpc]	$B_{\rm rms}^{\rm r}$ [G]	$B_{\rm rms}^{\rm eq}$ [G]	$\mathcal{E}_{\rm GW}$	$h_0^2\Omega_{\rm GW}$
A	0.15	3.8×10^{8}	5.8×10^{-8}	3.0×10^{-2}	3.0×10^{-7}	4.2×10^{-10}	2.2×10^{-6}	4.3×10^{-11}
B	10	2.8×10^{10}	3.2×10^{-10}	2.9×10^{-3}	2.9×10^{-7}	9.6×10^{-11}	5.3×10^{-7}	9.2×10^{-12}
C	460	1.4×10^{12}	8.0×10^{-12}	9.9×10^{-4}	3.8×10^{-7}	3.4×10^{-11}	5.3×10^{-7}	8.5×10^{-12}
D	3×10^{5}	9.0×10^{14}	4.5×10^{-14}	4.2×10^{-4}	3.4×10^{-7}	3.5×10^{-12}	1.4×10^{-5}	2.2×10^{-10}

in the nonhelical case. Except for the scale-invariant scaling in Run C at superhorizon scales, this leads to extremely blue spectra of electric and magnetic fields. Nevertheless, the total stress has still always a purely white noise spectrum and therefore also the GW field has a white noise spectrum below its peak value. Furthermore, for runs with large values of β, the onset of the drop toward larger frequencies is much sharper in runs with helicity than without. These aspects can have observational consequences. In particular, there would be more power at small wavenumbers and frequencies. On the other hand, for a certain magnetic energy, helical magnetogenesis produces somewhat weaker GWs than nonhelical magnetogenesis. However, as we have shown here, the appropriate scaling is not with $\mathcal{E}_{\rm M}$, but with $\mathcal{E}_{\rm EM}$, and therefore this conclusion is reversed. In fact, the fractional contribution of electric fields to the stress is much weaker in the helical case than without.

When studying GW generation from the CME, it was anticipated that some general features or behaviors would carry over to other magnetogenesis scenarios. In magnetogenesis from the CME, the GW energy was well described by a relation $\mathcal{E}_{\rm GW}=(q_{\rm M}\mathcal{E}_{\rm M}/k_{\rm c})^2$, where the efficiency $q_{\rm M}$ depended on the value of the conductivity and it also depended on which of the two possible regimes one is in. The possibility of two different regimes seems to be a special property of the CME that has not yet been encountered in other magnetogenesis scenarios. Also the presence of a conservation law of total chirality in the CME has no obvious counterpart in inflationary magnetogenesis, where magnetic helicity conservation is not obeyed during magnetogenesis in step I.

On the other hand, both the CME and helical inflationary magnetogenesis can produce circularly polarized GWs. However, the CME operates only on very small length scales that are in practice much smaller than what is shown in Figure 8, where an unphysically large chiral chemical potential was applied, just to see what GW strengths would then be possible. This naturally raises the question whether some combination of CME and inflationary magnetogenesis could produce either stronger or larger scale magnetic fields. A problem lies in the fact that the CME requires electric conductivity. It could therefore only be an effect that operates *after* inflationary magnetogenesis and during the radiation-dominated era. It could then enhance the magnetic field, but the resulting additional magnetic field would then only be of short length scales. Nevertheless, the preceding inflationary stage could lead to somewhat stronger fields and could thereby also produce stronger GWs. Another interesting effect could be the intermediate production of an imbalance of fermions from the magnetic field produced by inflationary magnetogenesis. This aspect has recently been explored by Hirono et al. (2015) and, in particular, by Schober et al. (2020) who showed that this effect is indeed only an intermediate one, because at late times, the chiral imbalance always gets converted back into magnetic fields.

When comparing a plot of $\mathcal{E}_{\rm GW}$ versus $\mathcal{E}_{\rm M}$ from inflationary magnetogenesis, the work of BS has shown that a scaling of the form $\mathcal{E}_{\rm GW}\propto\mathcal{E}_{\rm M}^2$ was obtained. Our new results for helical inflationary magnetogenesis explicitly confirm a $1/k_{\rm c}$ dependence, but here with $\mathcal{E}_{\rm GW}=(q_{\rm EM}\mathcal{E}_{\rm EM}/k_{\rm c})^2$, where $q_{\rm EM}$ shows only a very weak dependence on β. Here, $k_{\rm c}=k_*(1)$ has been used (as in BS), and $q_{\rm EM}=1$–2 has been found as a fit parameter. Note, however, that the formula for $\mathcal{E}_{\rm GW}$ in terms of $\mathcal{E}_{\rm EM}$ is entirely empirical. It would be important to produce some more robust analytic justification or refinements to this expectation.

Of observational interest may also be the profile and slope with which $\mathcal{P}_{\rm GW}(k)$ increases at low k. Interestingly, the fractional polarization continues to be nearly 100% for a range of wavenumbers around the GW peak at $2k_*(1)$, but shows a decline for small k.

We thank the referee for insightful remarks and Tina Kahniashvili and Kandaswamy Subramanian for useful discussions on the subject. Nordita's support during the program on Gravitational Waves from the Early Universe in Stockholm in 2019 is gratefully acknowledged. This work was support through grants from the Swedish Research Council (Vetenskapsradet, 2019-04234). We acknowledge the allocation of computing resources provided by the Swedish National Allocations Committee at the Center for Parallel Computers at the Royal Institute of Technology in Stockholm and Linköping.

Table 5. Model parameters for different values of $T_{\rm r}$.

$T_{\rm r}$	α	γ	$\mathcal{E}_{\rm EM}$	$H_{\rm f}$ [GeV]	$N_{\rm r}$	N	β	$g_{\rm r}$	$E_{\rm M}(\eta_{\rm ini}, k)$
10 GeV	2	1	0.07	2.3×10^{-11}	8.1	31.1	7.7	86	$\propto k^3$
8 GeV	2	1	0.01	2.8×10^{-11}	8.6	31.1	7.3	86	$\propto k^3$
120 MeV	2	1	0.01	1.2×10^{-3}	26.5	35.5	2.7	20	$\propto k^3$
150 MeV	2	1	0.006	2.7×10^{-4}	24.5	35.1	2.9	61.75	$\propto k^3$
460 GeV	−3	2.5	0.01	1.7×10^{-8}	7.3	32.9	3	106.75	$\propto k^{-1}$
3×10^5 GeV	1	1	0.01	10^{14}	32.1	53.4	1.7	106.75	$\propto k^5$

Software and Data Availability. The source code used for the simulations of this study, the PENCIL CODE (Pencil Code Collaboration et al. 2021), is freely available on https://github.com/pencil-code/. The DOI of the code is https://doi.org/10.5281/zenodo.2315093 `v2018.12.16` (Brandenburg 2018). The simulation setup and the corresponding data are freely available on doi:10.5281/zenodo.5137202; see also https://www.nordita.org/~brandenb/projects/HelicalMagnetoGene for easier access of the same material as on the Zenodo site.

APPENDIX

A. RELATION BETWEEN β AND THE REHEATING TEMPERATURE

We discussed in Section 2.3 various combinations of model parameters β and γ for a chosen value of $T_{\rm r}$. For the nonhelical case with $\gamma = 0$, details were already given in Appendix A of BS. The expression corresponding to Equation (A1) of BS is obtained as follows.

Details of the helical magnetogenesis model are explained in SSS. The expressions below their Equations (23) and (29) represent the solution for the scaled vector potential $\mathcal{A}_h$ during inflation and the matter-dominated era, respectively, and are given by

$$\mathcal{A}_{1h}(\eta) = \frac{e^{-h\pi\alpha/2}}{\sqrt{2k}} W_{i\alpha h,\alpha+\frac{1}{2}}(2ik\eta), \tag{A1}$$

$$\mathcal{A}_{2h}(\zeta) = d_1 M_{2i\beta h,-(2\beta+\frac{1}{2})}(2ik\zeta) + d_2 M_{2i\beta h,2\beta+\frac{1}{2}}(2ik\zeta). \tag{A2}$$

Here $h = \pm 1$, ζ is a time variable during the matter-dominated era defined in SSS as $\zeta \equiv \eta - 3\eta_{\rm f}$, where $\eta_{\rm f}$ is the value of conformal time at the end of inflation, and W and M represent the Whittaker functions of the first and second kind. The coefficients d_1 and d_2 are obtained by the matching $A_h \equiv \mathcal{A}_h/f$ and its derivatives at the end of inflation. In SSS, only the $\mathcal{A}_h$ in the superhorizon limit during the matter-dominated era was considered. Since this solution does not incorporate the extra growth of the modes when they start entering the horizon (as evident from Figure 2), we consider the full solution given in Equation (A2) in the present paper. By considering the full solution, we obtain d_1 and d_2 and, further using Equation (29) in Equations (17) and (18) of SSS, we obtain the magnetic and electric energy densities during the matter-dominated era. Demanding that the total EM energy be smaller than the background energy density at the end of inflation, we calculate the value of the Hubble parameter during inflation, $H_{\rm f}$, for given values of $T_{\rm r}$, α, and $\mathcal{E}_{\rm EM}$. Further, using these values, we estimate the value of $\beta \equiv 2N/N_r$, where N and N_r are the number of e-folds during inflation and the post-inflationary matter-dominated era, respectively. We provide these values in Table 5 along with the initial magnetic field spectrum in the superhorizon limit during the matter-dominated era and the value of the relativistic degrees of freedom at the beginning of the radiation-dominated era, $g_{\rm r}$.

REFERENCES

Adshead, P., Giblin, J. T., Scully, T. R., & Sfakianakis, E. I. 2016, JCAP, 2016, 039, doi: 10.1088/1475-7516/2016/10/039

Adshead, P., Giblin, J. T., & Weiner, Z. J. 2018, PhRvD, 98, 043525, doi: 10.1103/PhysRevD.98.043525

Amaro-Seoane, P., Audley, H., Babak, S., et al. 2017, arXiv e-prints, arXiv:1702.00786. https://arxiv.org/abs/1702.00786

Anand, S., Bhatt, J. R., & Pandey, A. K. 2019, EPJC, 79, 119, doi: 10.1140/epjc/s10052-019-6619-5

Anber, M. M., & Sorbo, L. 2006, JCAP, 2006, 018, doi: 10.1088/1475-7516/2006/10/018

Arzoumanian, Z., Baker, P. T., Blumer, H., et al. 2020, ApJL, 905, L34, doi: 10.3847/2041-8213/abd401

Banerjee, R., & Jedamzik, K. 2004, PhRvD, 70, 123003, doi: 10.1103/PhysRevD.70.123003

Barnaby, N., Namba, R., & Peloso, M. 2011, JCAP, 2011, 009, doi: 10.1088/1475-7516/2011/04/009

Biskamp, D., & Müller, W.-C. 1999, PhRvL, 83, 2195, doi: 10.1103/PhysRevLett.83.2195

Boyarsky, A., Fröhlich, J., & Ruchayskiy, O. 2012, PhRvL, 108, 031301, doi: 10.1103/PhysRevLett.108.031301

—. 2015, PhRvD, 92, 043004, doi: 10.1103/PhysRevD.92.043004

Brandenburg, A. 2018, Pencil Code, v2018.12.16, Zenodo, doi: 10.5281/zenodo.2315093

Brandenburg, A., & Boldyrev, S. 2020, ApJ, 892, 80, doi: 10.3847/1538-4357/ab77bd

Brandenburg, A., Clarke, E., He, Y., & Kahniashvili, T. 2021a, PhRvD, 104, 043513, doi: 10.1103/PhysRevD.104.043513

Brandenburg, A., Enqvist, K., & Olesen, P. 1996, PhRvD, 54, 1291, doi: 10.1103/PhysRevD.54.1291

Brandenburg, A., Gogoberidze, G., Kahniashvili, T., et al. 2021b, CQGra, 38, 145002. https://arxiv.org/abs/2103.01140

Brandenburg, A., He, Y., Kahniashvili, T., Rheinhardt, M., & Schober, J. 2021c, ApJ, 911, 110 (BHKRS), doi: 10.3847/1538-4357/abe4d7

Brandenburg, A., & Kahniashvili, T. 2017, PhRvL, 118, 055102, doi: 10.1103/PhysRevLett.118.055102

Brandenburg, A., Kahniashvili, T., Mandal, S., et al. 2017, PhRvD, 96, 123528, doi: 10.1103/PhysRevD.96.123528

Brandenburg, A., & Sharma, R. 2021, ApJ, in press, arXiv:2106.03857 (BS). https://arxiv.org/abs/2106.03857

Campanelli, L. 2009, IJMPD, 18, 1395, doi: 10.1142/S0218271809015175

Caprini, C., & Sorbo, L. 2014, JCAP, 2014, 056, doi: 10.1088/1475-7516/2014/10/056

Caprini, C., Hindmarsh, M., Huber, S., et al. 2016, JCAP, 2016, 001, doi: 10.1088/1475-7516/2016/04/001

Cheng, S.-L., Lee, W., & Ng, K.-W. 2016, PhRvD, 93, 063510, doi: 10.1103/PhysRevD.93.063510

Christensson, M., Hindmarsh, M., & Brandenburg, A. 2001, PhRvE, 64, 056405, doi: 10.1103/PhysRevE.64.056405

Cornwall, J. M. 1997, PhRvD, 56, 6146, doi: 10.1103/PhysRevD.56.6146

Demozzi, V., Mukhanov, V., & Rubinstein, H. 2009, JCAP, 8, 025, doi: 10.1088/1475-7516/2009/08/025

Detweiler, S. 1979, ApJ, 234, 1100, doi: 10.1086/157593

Domcke, V., Ema, Y., & Mukaida, K. 2020, JHEP, 2020, 55, doi: 10.1007/JHEP02(2020)055

Domcke, V., & Mukaida, K. 2018, JCAP, 2018, 020, doi: 10.1088/1475-7516/2018/11/020

Durrer, R., Hollenstein, L., & Jain, R. K. 2011, JCAP, 2011, 037, doi: 10.1088/1475-7516/2011/03/037

Durrer, R., & Neronov, A. 2013, Astron. Astrophys. Rev., 21, 62, doi: 10.1007/s00159-013-0062-7

Ellis, J., Fairbairn, M., Lewicki, M., Vaskonen, V., & Wickens, A. 2020, JCAP, 2020, 032, doi: 10.1088/1475-7516/2020/10/032

Ferreira, R. J. Z., Jain, R. K., & Sloth, M. S. 2013, JCAP, 2013, 004, doi: 10.1088/1475-7516/2013/10/004

Fujita, T., & Durrer, R. 2019, JCAP, 2019, 008, doi: 10.1088/1475-7516/2019/09/008

Fujita, T., Namba, R., Tada, Y., Takeda, N., & Tashiro, H. 2015, JCAP, 2015, 054, doi: 10.1088/1475-7516/2015/05/054

Garretson, W. D., Field, G. B., & Carroll, S. M. 1992, PhRvD, 46, 5346, doi: 10.1103/PhysRevD.46.5346

Gogoberidze, G., Kahniashvili, T., & Kosowsky, A. 2007, PhRvD, 76, 083002, doi: 10.1103/PhysRevD.76.083002

Hatori, T. 1984, JPSJ, 53, 2539, doi: 10.1143/JPSJ.53.2539

He, Y., Brandenburg, A., & Sinha, A. 2021, JCAP, 2021, 015, doi: 10.1088/1475-7516/2021/07/015

Hirono, Y., Kharzeev, D. E., & Yin, Y. 2015, PhRvD, 92, 125031, doi: 10.1103/PhysRevD.92.125031

Hobbs, G., Archibald, A., Arzoumanian, Z., et al. 2010, CQGra, 27, 084013, doi: 10.1088/0264-9381/27/8/084013

Joyce, M., & Shaposhnikov, M. 1997, PhRvL, 79, 1193, doi: 10.1103/PhysRevLett.79.1193

Kahniashvili, T., Brandenburg, A., Gogoberidze, G., Mandal, S., & Pol, A. R. 2021, PhRvR, 3, 013193, doi: 10.1103/PhysRevResearch.3.013193

Kahniashvili, T., Brandenburg, A., & Tevzadze, A. G. 2016, PhysS, 91, 104008, doi: 10.1088/0031-8949/91/10/104008

Kahniashvili, T., Gogoberidze, G., & Ratra, B. 2005, PhRvL, 95, 151301, doi: 10.1103/PhysRevLett.95.151301

Kahniashvili, T., Tevzadze, A. G., Brandenburg, A., & Neronov, A. 2013, PhRvD, 87, 083007, doi: 10.1103/PhysRevD.87.083007

Kamada, K., & Long, A. J. 2016, PhRvD, 94, 123509, doi: 10.1103/PhysRevD.94.123509

Kamada, K., Uchida, F., & Yokoyama, J. 2021, JCAP, 2021, 034, doi: 10.1088/1475-7516/2021/04/034

Kobayashi, T., & Afshordi, N. 2014, JHEP, 2014, 166, doi: 10.1007/JHEP10(2014)166

Kobayashi, T., & Sloth, M. S. 2019, PhRvD, 100, 023524, doi: 10.1103/PhysRevD.100.023524

Maggiore, M. 2000, PhR, 331, 283, doi: 10.1016/S0370-1573(99)00102-7

Mukhanov, V. F., Feldman, H. A., & Brandenberger, R. H. 1992, PhR, 215, 203, doi: 10.1016/0370-1573(92)90044-Z

Ng, K.-W., Cheng, S.-L., & Lee, W. 2015, Chin. J. Phys., 110105, doi: 10.6122/CJP.20150909

Okano, S., & Fujita, T. 2021, JCAP, 2021, 026, doi: 10.1088/1475-7516/2021/03/026

Pencil Code Collaboration, Brandenburg, A., Johansen, A., et al. 2021, JOSS, 6, 2807, doi: 10.21105/joss.02807

Pouquet, A., Frisch, U., & Leorat, J. 1976, JFM, 77, 321, doi: 10.1017/S0022112076002140

Ratra, B. 1992, ApJL, 391, L1, doi: 10.1086/186384

Roper Pol, A., Brandenburg, A., Kahniashvili, T., Kosowsky, A., & Mandal, S. 2020a, GApFD, 114, 130, doi: 10.1080/03091929.2019.1653460

Roper Pol, A., Mandal, S., Brandenburg, A., & Kahniashvili, T. 2021, JCAP, submitted, arXiv:2107.05356. https://arxiv.org/abs/2107.05356

Roper Pol, A., Mandal, S., Brandenburg, A., Kahniashvili, T., & Kosowsky, A. 2020b, PhRvD, 102, 083512, doi: 10.1103/PhysRevD.102.083512

Schober, J., Fujita, T., & Durrer, R. 2020, PhRvD, 101, 103028, doi: 10.1103/PhysRevD.101.103028

Sharma, R., Jagannathan, S., Seshadri, T. R., & Subramanian, K. 2017, PhRvD, 96, 083511, doi: 10.1103/PhysRevD.96.083511

Sharma, R., Subramanian, K., & Seshadri, T. R. 2018, PhRvD, 97, 083503 (SSS), doi: 10.1103/PhysRevD.97.083503

—. 2020, PhRvD, 101, 103526, doi: 10.1103/PhysRevD.101.103526

Subramanian, K. 2016, RPPh, 79, 076901, doi: 10.1088/0034-4885/79/7/076901

Taiji Scientific Collaboration, Wu, Y.-L., Luo, Z.-R., Wang, J.-Y., et al. 2021, CmPhy, 4, 34, doi: 10.1038/s42005-021-00529-z

Turner, M. S., & Widrow, L. M. 1988, PhRvD, 37, 2743, doi: 10.1103/PhysRevD.37.2743

Vachaspati, T. 2001, PhRvL, 87, 251302, doi: 10.1103/PhysRevLett.87.251302

Vilenkin, A. 1980, PhRvD, 22, 3080, doi: 10.1103/PhysRevD.22.3080